Unraveling Ultrafast Dynamics in Photoexcited Aniline

Gareth M. Roberts,[†] Craig A. Williams,[†] Jamie D. Young,[†] Susanne Ullrich,[‡] Martin J. Paterson,*[,§] and Vasilios G. Stavros*[,†]

[†]Department of Chemistry, University of Warwick, Library Road, Coventry, CV4 7AL, United Kingdom
[‡]Department of Physics and Astronomy, University of Georgia, Athens, Georgia 30602, United States
[§]Institute of Chemical Sciences, Heriot-Watt University, Edinburgh, EH14 4AS, United Kingdom

S *Supporting Information*

ABSTRACT: A combination of ultrafast time-resolved velocity map imaging (TR-VMI) methods and complete active space self-consistent field (CASSCF) ab initio calculations are implemented to investigate the electronic excited-state dynamics in aniline (aminobenzene), with a perspective for modeling $^1\pi\sigma^*$ mediated dynamics along the amino moiety in the purine derived DNA bases. This synergy between experiment and theory has enabled a comprehensive picture of the photochemical pathways/conical intersections (CIs), which govern the dynamics in aniline, to be established over a wide range of excitation wavelengths. TR-VMI studies following excitation to the lowest-lying $^1\pi\pi^*$ state ($1^1\pi\pi^*$) with a broadband femtosecond laser pulse, centered at wavelengths longer than 250 nm (4.97 eV), do not generate any measurable signature for $^1\pi\sigma^*$ driven N−H bond fission on the amino group. Between wavelengths of 250 and >240 nm (<5.17 eV), coupling from $1^1\pi\pi^*$ onto the $^1\pi\sigma^*$ state at a $1^1\pi\pi^*/^1\pi\sigma^*$ CI facilitates ultrafast nonadiabatic N−H bond fission through a $^1\pi\sigma^*/S_0$ CI in <1 ps, a notion supported by CASSCF results. For excitation to the higher lying $2^1\pi\pi^*$ state, calculations reveal a near barrierless pathway for CI coupling between the $2^1\pi\pi^*$ and $1^1\pi\pi^*$ states, enabling the excited-state population to evolve through a rapid sequential $2^1\pi\pi^* \to 1^1\pi\pi^* \to {}^1\pi\sigma^* \to$ N−H fission mechanism, which we observe to take place in 155 ± 30 fs at 240 nm. We also postulate that an analogous cascade of CI couplings facilitates N−H bond scission along the $^1\pi\sigma^*$ state in 170 ± 20 fs, following 200 nm (6.21 eV) excitation to the $3^1\pi\pi^*$ surface. Particularly illuminating is the fact that a number of the CASSCF calculated CI geometries in aniline bear an exceptional resemblance with previously calculated CIs and potential energy profiles along the amino moiety in guanine, strongly suggesting that the results here may act as an excellent grounding for better understanding $^1\pi\sigma^*$ driven dynamics in this ubiquitous genetic building block.
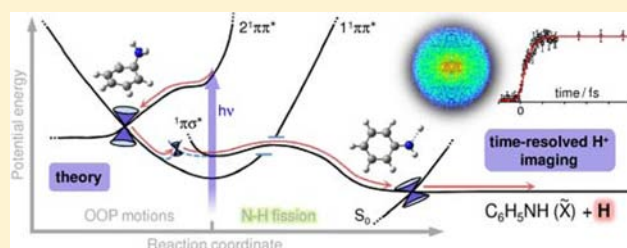
1. INTRODUCTION

Recent years have seen numerous studies carried out to gain a greater understanding of the excited electronic state dynamics in a wide range of heteroaromatics (e.g., phenols, indoles, and pyrroles).[1,2] To a large extent, this has been triggered because of their notable roles as ultraviolet (UV) chromophores in biologically relevant species, such as DNA bases and aromatic amino acids.[3,4] This class of heteroaromatic biomolecules is notorious for exhibiting a high degree of photostability (a beneficial aversion to photoinduced fragmentation/excited-state reactions) following the absorption of potentially harmful UV radiation, manifesting in low fluorescence quantum yields and short excited-state lifetimes.[4] It has been proposed that photostable behavior is a critical characteristic for these molecular 'building-blocks' of life; in the present day, they can act as highly efficient 'UV sunscreens' which minimize the formation of genetic mutations (photolesions) in DNA,[4,5] while on the prebiotic earth, which lacked any ozone shielding from extraterrestrial UV radiation, it has been conjectured that UV photostability acted as a 'photochemical funnel' for selecting stable species,[6,7] suitable for founding basic self-replicating molecular systems and, subsequently, early forms of life.

The origins of efficient UV photostability in heteroaromatics (and aromatic biomolecules) have been rationalized by invoking ultrafast nonadiabatic dynamics, occurring on the order of tens to hundreds of femtoseconds (fs), via conical intersections (CIs) between electronic excited states and the electronic ground state (S_0).[8−17] This photochemistry effectively transforms potentially destructive UV photon energy into a thermally (vibrationally) excited S_0 state, allowing nascent heat to be harmlessly dissipated into the surrounding environment (e.g., a solvent bath). A synergy between both experiment and theory has been implemented over the past decade in an effort to effectively characterize these rapid molecular relaxation pathways.[18] One prominent mechanism emerging from the theoretical studies of Sobolewski et al. has since received considerable attention.[19] Sobolewski et al. proposed that following initial excitation of optically 'bright' $^1\pi\pi^*$ excited states in the vertical Franck−Condon (vFC) region, population may couple through a CI onto dissociative $^1\pi\sigma^*$ states, localized along heteroatom-hydride coordinates (X-

H, where X = N or O) and facilitate either rapid repopulation of S_0 via a $^1\pi\sigma^*/S_0$ CI at extended X-H bond lengths or ultrafast X-H bond fission (and subsequent recombination in hydrogen-bonded motifs, such as DNA base pairs).[18] It is important to highlight for context, however, that $^1\pi\sigma^*$ states offer one of an ensemble of nonradiative relaxation mechanisms in heteroaromatic biomolecules, as demonstrated by studies on individual DNA bases.[20]

In this article, we comprehensively investigate nonadiabatic dynamics in aniline (aminobenzene; its structure is shown in the Figure 1 inset), with particular focus on $^1\pi\sigma^*$ mediated
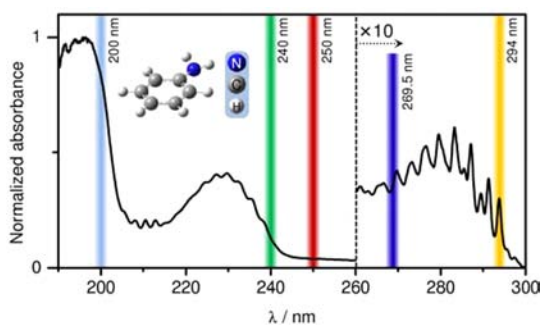

Figure 1. Vapor-phase UV absorption spectrum of aniline (molecular structure inset). Labeled bands indicate pump excitation wavelengths used in the ultrafast TR-VMI experiments: 294 (yellow), 269.5 (blue), 250 (red), 240 (green), and 200 nm (light blue) center wavelengths.

behavior localized to the NH_2 group. Aniline, together with its chemical derivatives, can be seen as exceptionally valuable candidates for modeling the photochemistry along the amino moiety in the purine derived DNA bases guanine and adenine[21,22] (particularly in highly differential gas-phase measurements), while many substituted aminobenzenes have long been seen as a cornerstone for intricately understanding intramolecular charge-transfer (ICT) dynamics in more complex species.[23–25] To date, a number of experimental[21,26–32] and theoretical[33–38] investigations have studied aniline's spectroscopy. However, few experimental studies have been conducted to thoroughly understand its ultrafast excited-state dynamics,[39,40] whereas to the best of our knowledge, no high-level ab initio calculations have been performed to classify the CIs that drive this behavior. Here, we address both of these issues to provide a new and significantly more detailed perspective of the photochemistry occurring in this valuable model aromatic heterocycle.

Spectroscopically, the vapor-phase UV absorption spectrum of aniline (Figure 1) is dominated by features arising from excitation to a number of optically 'bright' $^1\pi\pi^*$ states. The lowest energy of these $\pi^* \leftarrow \pi$ transitions, hereon termed $1^1\pi\pi^*$, is predicted to have an absorption onset of ~4.2 eV (294 nm),[36] which agrees with the experimentally observed absorption onset in Figure 1. Symmetry adapted cluster/configuration interaction (SAC-CI) calculations by Honda et al.[36] also determine higher lying $^1\pi\pi^*$ states, $2^1\pi\pi^*$ and $3^1\pi\pi^*$, located at vertical excitation energies of 5.34 eV (232 nm) and 6.62 eV (187 nm), respectively. These energies also correlate reasonably well with the observed onsets for absorption increases in Figure 1 at ~240 nm ($2^1\pi\pi^* \leftarrow S_0$) and ~205 nm ($3^1\pi\pi^* \leftarrow S_0$). In addition to these $^1\pi\pi^*$ states, Honda et al. indentify the signature of a $^1\pi\sigma^*$ state.[36] In the vFC region, this $^1\pi\sigma^*$ state exhibits notable 3s Rydberg character associated with

the nitrogen (N) atom (resulting from strong mixing with the $^1\pi3s \leftarrow S_0$ transition) and possesses a negligible one-photon oscillator strength. In the ground state C_s symmetry though, the $^1\pi\sigma^*$ $(A') \leftarrow S_0$ (A') transition is formally electric dipole allowed $(A' \otimes a' \otimes A' = A')$, but traditionally, absorption to these states is very weak. The presence of this $^1\pi\sigma^*$ state was concomitantly confirmed by Ebata et al. through (2 + 2) resonance enhanced multiphoton ionization (REMPI) measurements.[31] These experiments revealed a sharp onset for the $^1\pi\sigma^*$ state at ~4.6 eV (269.5 nm), indicating a quasi-bound character to this state in the vFC region, due to the strong mixing with the $^1\pi3s$ Rydberg state, which evolves into a dissociative potential, defined by the valence σ^* character, upon N−H bond extension enabling N−H bond scission (see schematic potentials presented later in the article).

More recently, dynamics involving the $^1\pi\sigma^*$ surface have been investigated in the frequency domain using both multimass ion imaging[32] and high-resolution H-atom Rydberg tagging techniques.[21] In combination, these studies reveal that following excitation at <269 nm N−H bond fission via the $^1\pi\sigma^*$ state is active, generating H-atoms with high amounts of kinetic energy (KE) together with anilino (C_6H_5NH) radical cofragments in their electronic ground state ($\tilde{X}$). Further to this, ultrafast time-domain experiments by Montero et al.,[39] performed using time-resolved ion yield (TR-IY) measurements on the aniline parent cation (aniline$^+$), were able to extrapolate lifetimes for the $^1\pi\sigma^*$ state, all of which were between 145−165 fs across the 234−265 nm excitation range. At wavelengths longer than 269 nm, both time[39] and frequency[21,32] domain studies observed no signatures for $^1\pi\sigma^*$ mediated N−H dissociation, in accord with the excitation onset of the $^1\pi\sigma^*$ state.

We herein report detailed new experimental results which probe the time scales for $^1\pi\sigma^*$ mediated N−H bond scission in isolated (gas-phase) aniline following excitation at multiple wavelengths over the range 294−200 nm. The results presented provide a direct signature of the $^1\pi\sigma^*$ driven H-atom elimination dynamics; by combining ultrafast pump−probe spectroscopy[41] and velocity map ion imaging (time-resolved velocity map imaging, TR-VMI),[42] we critically extract both temporal and energetic information pertaining to the N−H bond fission process by selectively probing the H-atom photoproducts with a (2 + 1) REMPI technique. This approach provides compelling evidence that N−H dissociation along the $^1\pi\sigma^*$ state does indeed occur within an ultrafast (fs) time frame. Interpretation of these results is guided by high-level ab initio calculations, which, for the first time, provide new and invaluable insights into CI pathways in aniline, through which ultrafast population transfer between electronic states can occur.

2. METHODS

2.1. Experiment. The setup utilized to probe the photochemistry of aniline has been reported in detail previously[43] and further information is provided in the Supporting Information (SI). Briefly, aniline (Sigma-Aldrich, > 98%) is seeded in helium (~2 bar) and introduced into a velocity map imaging spectrometer using an Even-Lavie pulsed valve[44] which is heated to ~100 °C. A commercial amplified Ti:Sapphire fs laser system (Spectra-Physics, Spitfire XP) is used to generate fundamental pulses (~35 fs duration) centered at 800 nm with an energy of 3 mJ/pulse in a 1 kHz pulse train, which are then up-converted into the UV regime with appropriate frequency mixing techniques. Specifically, dynamics are initiated using fs laser pulses

Table 1. Calculated Vertical (ΔE_{vert}) and Adiabatic (ΔE_{ad}) Excitation Energies for Aniline at the TD-CAM-B3LYP/aug-cc-pVTZ, EOM-CCSD/aug-cc-pVDZ, CAS1/6-311+G(d), and CAS2/6-311+G(d) Levels (CAS1 = CASSCF(8,7) and CAS2 = CASSCF(10,9))[a]

| state | ΔE_{vert}/eV | | | | ΔE_{ad}/eV | | |
	TD-CAM-B3LYP (f)	EOM-CCSD (f)	CAS1	CAS2	CAS1	CAS2	expt
$1^1\pi\pi^*$	4.88 (0.036)	4.71 (0.026)	4.86	4.85	4.66	4.64	4.22[b]
$^1\pi\sigma^*$	4.96 (0.007)	4.90 (0.006)	–	5.78[d]	–	–	4.61[c]
$2^1\pi\pi^*$	5.53 (0.099)	5.75 (0.158)	7.32[d]	8.13[d]	6.81[d]	–	~5.10
$3^1\pi\pi^*$	6.61 (0.220)	6.72 (0.249)	–	–	–	–	~6.05

[a]Values in parentheses correspond to calculated oscillator strengths (f). Experimental energies (expt) for the electronic states are also provided in units of eV. [b]Refs 21 and 28. [c]Ref 31. [d]State-averaged energies.

($h\nu_{pu}$) generated by optical parametric amplification (Light Conversion, TOPAS-C) over the range 294−240 nm (~5−6 μJ/pulse), while 200 nm fs laser pulses (~1 μJ/pulse) are created using a series of type-I and -II β-barium borate (BBO) crystals. Any nascent H-atoms subsequently undergo (2 + 1) REMPI as a function of time (Δt), using temporally delayed fs pulses centered at 243 nm ($h\nu_{pr}$), two photons of which are resonant with the two-photon allowed 2s ← 1s transition in H. $h\nu_{pr}$ is generated with a second optical parametric amplifier (Light Conversion, TOPAS-C). H$^+$ is then detected as a function of both time and KE using TR-VMI. The desired total kinetic energy release (TKER) spectra are derived from the measured H$^+$ velocity map images using a polar onion-peeling algorithm,[45] together with an appropriate Jacobian and calibration factor,[46] assuming C_6H_5NH (92 amu) as the radical cofragment of the dissociation process. For these experiments, the Gaussian laser cross-correlation was measured to be ~160 fs full width at half-maximum (fwhm) between 200 and 243 nm pulses and ~120 fs fwhm for pump wavelengths between 294 and 240 nm with 243 nm.

A vapor-phase absorption spectrum (shown in Figure 1) over the range 300−190 nm was recorded using a commercial UV−vis absorption spectrometer (PerkinElmer, Lambda 25, 1 nm resolution) by heating aniline to ~80 °C inside a fused silica sample tube.

2.2. Computational Details. All calculations have been performed using the Gaussian computational suite.[47,48] The equation-of-motion coupled cluster singles and doubles (EOM-CCSD) method[49] and time-dependent (TD) density functional theory, with the CAM-B3LYP functional,[50] were used to evaluate the vertical excitation energies (ΔE_{vert}) of the $^1\pi\pi^*$ and $^1\pi\sigma^*$ electronic excited states of aniline, together with their oscillator strengths (f), using aug-cc-pVDZ and aug-cc-pVTZ basis sets, respectively. Initial geometry optimized ground state (S_0) structures for EOM-CCSD calculations were obtained using density functional theory (B3LYP functional), whereas TD-CAM-B3LYP calculations were fully geometry optimized using CAM-B3LYP. Both S_0 geometry optimizations used an aug-cc-pVDZ basis. For excitation energies, the EOM-CCSD formalism is equivalent to linear response coupled cluster (CCSD) theory, while the CAM-B3LYP functional has been selected as it combines the hybrid qualities of the popular B3LYP functional but also compensates for its short-comings through the addition of a long-range corrected exchange functional;[50] specifically, the amount of exact exchange included rises as the interelectronic distance increases. In particular, CAM-B3LYP vastly improves the description of excited states with significant Rydberg or ICT character, compared to B3LYP, which is notorious for performing poorly at this type of photochemical problem.[51,52] In aniline, the $^1\pi\sigma^*$ state exhibits strong Rydberg character in the vFC region, while some of the excited $^1\pi\pi^*$ states in aniline possess ICT character.

To explore the excited-state potential energy surfaces in aniline the complete active space self-consistent field (CASSCF) formalism was implemented. All CASSCF calculations have been performed using a 6-311+G(d) Pople basis set. The CASSCF method is used here to generate qualitatively correct wave functions around the CI regions of the potential energy landscape, where nonadiabatic dynamics are most probable. We note that CASSCF calculations lack any description of dynamic correlation effects, and the EOM-CCSD and TD-CAM-

B3LYP calculations serve as a 'benchmark' against which the CASSCF results can be compared/verified, particularly in the vFC region in which they are valid. The orbital rotation derivatives were negated from the solutions of the coupled perturbed multiconfigurational self-consistent field (CPMCSCF) equations when performing CI searches. Equally state-averaged orbitals, between the upper and lower states involved in CIs, were used in all CI searches. Equal state averaging with the state immediately lower in energy was also implemented to calculate the vertical and adiabatic excitation energies (ΔE_{ad}) of the $^1\pi\sigma^*$ and $2^1\pi\pi^*$ excited states. Specific details of X-electron/Y-orbital active space (X,Y) selections are provided with results in Section 3.1, where X and Y are the number of electrons and orbitals in the active space, respectively.

Valence π bonding (VB) structures in the excited states were determined by analyzing the spin-exchange density (P_{ij}) with localized active space orbitals,[53] which also provides access to the localized one-electron density matrix (D_{ii}). Localized active space orbitals were obtained using the method previously described by Boys.[54] The P_{ij} matrix elements aid to understand the spin coupling within the molecule, and this methodology has previously been reported in detail by Blancafort et al.[55] (see ref 56 for an example of using this method to determine excited-state VB structures). From a chemical perspective, positive P_{ij} values correspond to a singlet coupling, indicating a π bonding character, while negative values correlate to a triplet coupling, implying a lack of π bonding; for comparison, P_{ij} values in benzene are ~0.34.[55] When computed P_{ij} values for the excited states are compared with those of the ground state, changes to the bonding order of the excited states can be obtained. Additionally, the diagonal elements of the one-electron density matrix, D_{ii}, enable one to assess the degree and nature of any ICT in the excited states.[57]

3. RESULTS AND DISCUSSION

3.1. Ab Initio Calculations. We initially report the results of EOM-CCSD, TD-CAM-B3LYP, and CASSCF computations, which will provide context for interpreting the experimental TR-VMI results discussed in Section 3.2.

3.1.1. Vertical Excitation Energies. The results of EOM-CCSD and TD-CAM-B3LYP calculations are presented in Table 1. For both methods the computed ΔE_{vert} and f values of the $1^1\pi\pi^*$, $^1\pi\sigma^*$, $2^1\pi\pi^*$, and $3^1\pi\pi^*$ states are: (i) in good quantitative agreement with each other; (ii) in reasonable accord with previous SAC-CI values,[36] acknowledging that both the EOM-CCSD and TD-CAM-B3LYP ΔE_{vert} values are marginally greater; (iii) comparable to the experimentally determined excitation onsets for these states (see Table 1) obtained from the absorption spectrum in Figure 1 and previous REMPI measurements;[29,31] and finally (iv) generate f values which increase from the lowest $1^1\pi\pi^*$ to the higher $3^1\pi\pi^*$ state, mirroring the sizable increases in absorbance at the experimentally assigned onsets for these states in Figure 1. As an aside, the agreement across the TD-CAM-B3LYP, EOM-CCSD, and SAC-CI results also demonstrates the strength of

the CAM-B3LYP functional for tackling excited states with notable Rydberg character, such as the $^1\pi\sigma^*$ state here, and $2^1\pi\pi^*$ which is an ICT state (confirmed through analysis of D_{ii} from CASSCF calculations in Section 3.1.2).

3.1.2. Excited-State Minimum-Energy Structures and Valence Bonding.

CASSCF calculations have been performed to explore both the equilibrium structures and the VB configurations for S_0, in addition to ΔE_{vert}, equilibrium structures, VB, and ΔE_{ad} for the excited $1^1\pi\pi^*$ and $2^1\pi\pi^*$ states (all CASSCF calculated geometries are provided in the SI). An 8 electrons in 7 orbitals (8,7) active space (hereon referred to as CAS1), consisting of the 3 π orbitals, the N-atom lone pair (n), which is heavily conjugated into the ring π system, and the three corresponding π^* orbitals (see Figure S1 in the SI for orbital hypersurfaces) was used to calculate the S_0 equilibrium geometry. This size active space gives rise to 490 singlet configuration state functions. The result of the S_0 geometry optimization ($S_{0\ min}$) generates a structure, presented in Figure 2a, where the plane of the NH_2 group lies at an angle
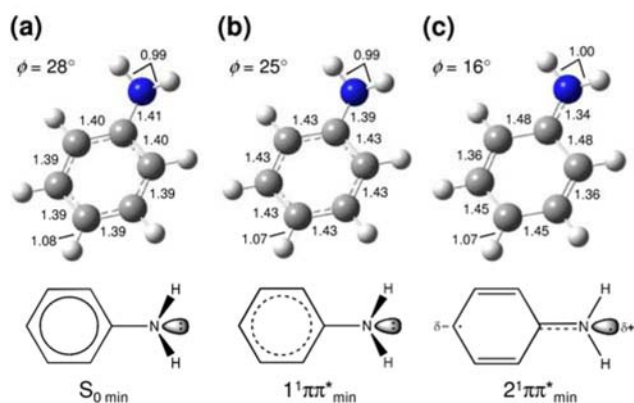

Figure 2. Calculated minimum energy structures for (a) $S_{0\ min}$, (b) $1^1\pi\pi^*_{min}$, and (c) $2^1\pi\pi^*_{min}$ at the CAS1/6-311+G(d) level. Calculated valence bonding structures for the S_0, $1^1\pi\pi^*$, and $2^1\pi\pi^*$ excited states are also provided.

(ϕ) of ~28° with respect to the benzene ring plane, forming a pyramidal structure, in reasonable accord with previous findings.[28,36]

The CAS1 space was also used to determine properties of the $1^1\pi\pi^*$ state. The value determined for ΔE_{vert} for the $1^1\pi\pi^* \leftarrow S_0$ transition is provided in Table 1 (4.86 eV) and is in excellent agreement with the EOM-CCSD and TD-CAM-B3LYP results, as one would expect for a state of the nature shown in Figure 2. Figure 2b displays the calculated minimum energy structure of the $1^1\pi\pi^*$ state ($1^1\pi\pi^*_{min}$) which adiabatically lies 4.66 eV (Table 1) above the $S_{0\ min}$ structure both calculated with the same active space. Previous theoretical calculations[36] and high-resolution measurements[28] have proposed that aniline undergoes a pyramidal to quasi-planar rearrangement upon excitation from S_0 to $1^1\pi\pi^*$, analogous to the photoinduced rearrangement in the prototypical amine ammonia[43,58] (N.B., in ammonia the first excited singlet electronic state possesses $^1n\sigma^*$ character rather than $^1\pi\pi^*$). At the CAS1/6-311+G(d) level the $1^1\pi\pi^*_{min}$ structure is similar to the $S_{0\ min}$ structure (see Figure 2), with some ring breathing deformation of the phenyl ring (all C−C bonds elongated from ~1.40 to ~1.43 Å) and only a small reduction in ϕ from ~28° to ~25°. Such a result is corroborated through a VB analysis of the $1^1\pi\pi^*$ state using the spin-exchange density, P_{ij}, with localized active space orbitals

and the one-electron density matrix, whose diagonal elements, D_{ii}, give the relative occupations of the localized orbitals (both π and n orbitals for CAS1).[56] Calculated P_{ij} and D_{ii} values are provided in Tables S1 and S2 in the SI, respectively, for both S_0 and $1^1\pi\pi^*$. The VB representations arising from the CAS1 calculations for S_0 and $1^1\pi\pi^*$ are presented in Figure 2, revealing that the $1^1\pi\pi^*$ state exhibits less π-bonding character on the phenyl ring relative to S_0, in line with the aforementioned ring breathing motion calculated for the $1^1\pi\pi^* \leftarrow S_0$ transition. These VB structures for S_0 and $1^1\pi\pi^*$ are akin to the Kekulé and anti-Kekulé structures, respectively, seen in benzene for the analogous electronic states.[18,55] In further support of our calculations, we note that: (i) the calculated rotational constants for the $1^1\pi\pi^*_{min}$ structure compare reasonably well with the experimentally determined values (see ref 59); and (ii) this structure is comparable to previously calculated minima for $1^1\pi\pi^*$ states (exhibiting equivalent VB structures) in substituted aminobenzenes.[23] This therefore leads us to propose that the $1^1\pi\pi^*_{min}$ may not be planar, but we do highlight that our calculations do not take into account the energy barrier to inversion in $1^1\pi\pi^*$, which, if small, could very well lead to the experimental observation of a time averaged quasi-planar structure, as concluded previously by Sinclair and Pratt.[28]

The calculated CAS1 ΔE_{vert} value for the $2^1\pi\pi^*$ state is 7.32 eV, which is a notable 1.79 eV greater than the EOM-CCSD result and 1.57 eV larger than the TD-CAM-B3LYP calculation. The significant overestimation of ΔE_{vert} by the CAS1 computations originates from the fact that $2^1\pi\pi^*$ is an ICT state, as confirmed in the VB analysis below. It is well-established that the CASSCF method overestimates ICT excitations,[60,61] and such behavior may in principle be corrected through the inclusion of dynamic correlation effects. However, we stress that although CASSCF fails to describe the energetics of the $2^1\pi\pi^*$ state at a quantitative level, the key features of its potential energy landscape should remain qualitatively correct, as observed for investigations in related heteroaromatic species with analogous characteristics,[23,56,60,62] thus enabling important structures, such as local minima and CIs, to be located using analytical gradient driven techniques. With this in mind, a local (shallow) minimum energy structure of the $2^1\pi\pi^*$ state ($2^1\pi\pi^*_{min}$) is presented in Figure 2c and has an associated $\Delta E_{ad} = 6.81$ eV (Table 1). The use of the term 'local (shallow) minimum' for this structure is discussed below. Upon excitation from S_0 to the $2^1\pi\pi^*$ manifold, these calculations reveal that aniline undergoes a significant structural rearrangement, where the NH_2 moiety follows a pyramidal to near-planar shift ($\phi = 16°$) and the C−N bond becomes reduced in length from 1.40 Å in $S_{0\ min}$ to 1.34 Å at $2^1\pi\pi^*_{min}$. In combination, these two features suggest that the N-atom lone pair orbital becomes significantly mixed into the π-system of the benzene ring in $2^1\pi\pi^*$, resulting in an evolution toward C−N double bonding character. This interpretation is confirmed by comparing the calculated P_{ij} and D_{ii} values for the $2^1\pi\pi^*$ state with those of S_0 (Tables S1 and S2 in the SI) and gives rise to the VB structure also depicted in Figure 2c. As alluded to above, inspection of the D_{ii} values, relative to S_0, indicates that the $2^1\pi\pi^*$ manifold exhibits ICT character, with ~0.2 electrons transferred from the N-atom n orbital to the opposite end of the phenyl ring. This ICT is likely to be one of the driving forces behind the pyramidal to near-planar rearrangement observed for the $2^1\pi\pi^* \leftarrow S_0$ transition, as the now electron deficient n orbital tries to regain some electron density by more strongly mixing into the
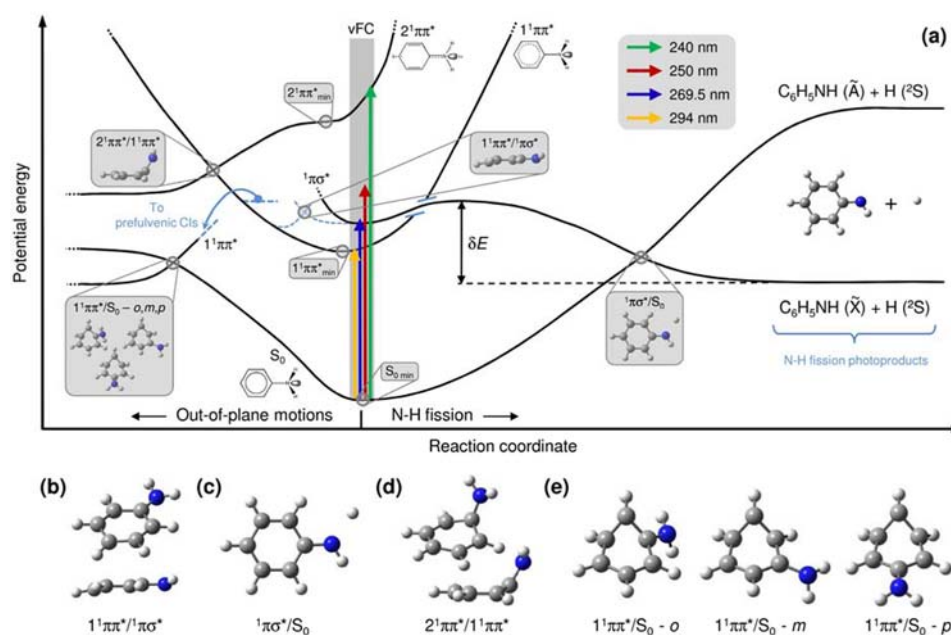
12581

dx.doi.org/10.1021/ja3029729 | J. Am. Chem. Soc. 2012, 134, 12578−12589

Figure 3. (a) Generic potential energy profiles of the S_0, $1^1\pi\pi^*$, $^1\pi\sigma^*$, and $2^1\pi\pi^*$ electronic states in aniline along the reaction coordinate (for both out-of-plane motions, left, and the N−H fission coordinate, right). Vertical yellow, blue, red, and green arrows in the vFC region signify excitation at 294, 269.5, 250, and 240 nm, respectively, in the TR-VMI experiments. Dashed light-blue lines represent pathways to electronic state couplings in other coordinates. The break in the $1^1\pi\pi^*$ state, shown by the solid blue lines, pictorially represents that there is no degeneracy between the $1^1\pi\pi^*$ and $^1\pi\sigma^*$ states at elongated N−H bond lengths. Significant calculated CASSCF geometries are labeled on the potentials. Calculated CI geometries are more clearly shown below for the (b) $1^1\pi\pi^*/^1\pi\sigma^*$, (c) $^1\pi\sigma^*/S_0$, (d) $2^1\pi\pi^*/1^1\pi\pi^*$, and (e) $1^1\pi\pi^*/S_0$-o,m,p prefulvenic CIs.

electron-rich π-system. At this stage, we highlight that the CASSCF geometry optimization in $2^1\pi\pi^*$, originating from the vFC region, initially evolves toward the reported local (shallow) $2^1\pi\pi^*_{min}$ geometry. However, in explanation of the term local (shallow) minimum, inspection of the forces (obtained from the analytical CASSCF gradient) in the $2^1\pi\pi^*_{min}$ region of the $2^1\pi\pi^*$ potential energy surface reveals that the $2^1\pi\pi^*_{min}$ structure is only very weakly bound. Thus, the potential is very flat in this region, and very small step sizes are required to converge the displacements. There is only a very small barrier from this minimum to a CI seam. As a result, further geometry optimization (using larger step sizes) leads to the structure relaxing further in energy toward a region of energetic degeneracy (a CI) between the $2^1\pi\pi^*$ and $1^1\pi\pi^*$ electronic states, which we explore in greater detail in Section 3.1.3.

3.1.3. Overview of CIs. Further to investigating the minimum energy structures and VB in aniline's excited states, the CASSCF formalism has been implemented to explore CIs between the lower-lying electronic states (S_0, $1^1\pi\pi^*$, $2^1\pi\pi^*$, and $^1\pi\sigma^*$) which may facilitate ultrafast population transfer. Despite the qualitative nature of the CASSCF approach, previous studies on other aromatic/aliphatic systems have shown that CASSCF studies can provide a good guide to understanding many of the major mechanistic aspects of excited-state dynamics.[56,63,64]

The CAS1 active space described in section 3.1.2 was used to isolate CIs involving the S_0, $1^1\pi\pi^*$, and $2^1\pi\pi^*$ surfaces, while a larger (10,9) space (designated CAS2), consisting of the CAS1 orbitals in addition to the corresponding N−H σ and σ^* orbitals, was constructed to explore CIs involving the $^1\pi\sigma^*$ and $1^1\pi\pi^*$ states. This larger CAS2 active space generates 5292 singlet configuration state functions. It computes the $^1\pi\sigma^*$ state to lie 5.78 eV vertically above the associated CAS2 $S_{0\,min}$ structure (see Table 1). Calculated ΔE_{vert} and ΔE_{ad} values for

$1^1\pi\pi^*$ using the larger CAS2 space are approximately unaltered from those determined with CAS1, whereas ΔE_{vert} for the higher lying $2^1\pi\pi^*$ state is raised in energy to 8.13 eV. The results of searches for minimum energy crossing points (MECPs) of CIs give rise to a mechanistic picture summarized by the generic potential energy profiles in Figure 3a. Also presented in Figure 3b−e are the calculated MECP structures associated with the CIs, whereas the branching space vectors for the CIs are depicted in Figure 4. These pairs of branching space motions are the two nuclear motions responsible for lifting the energetic degeneracy between the two electronic surfaces at the MECPs of the CIs, while the electronic state degeneracy is conserved in the remaining $3N − 8$ vibrational degrees of freedom (N = number of atoms).[18,65] The two modes correspond to the gradient of the energy difference between the two electronic states (GD) and the derivative coupling (DC) which is parallel to the nonadiabatic coupling gradient. The latter is typically responsible for driving nonadiabatic (vibronic) coupling between the two electronic states, causing population transfer through the CI.[65] The associated ΔE_{ad} energies for the MECPs of the CIs (relative to $S_{0\,min}$) are provided in Table 2.

3.1.4. CIs with the $^1\pi\sigma^*$ State. To begin, we consider CIs involving the $^1\pi\sigma^*$ state. These calculations reveal two CIs, the first between the $1^1\pi\pi^*$ and $^1\pi\sigma^*$ states ($1^1\pi\pi^*/^1\pi\sigma^*$) and the second between the $^1\pi\sigma^*$ and S_0 ground state ($^1\pi\sigma^*/S_0$). We focus initially on the $1^1\pi\pi^*/^1\pi\sigma^*$ CI, whose MECP geometry and branching space vectors are shown in Figures 3b and 4a, respectively. This CI is calculated to adiabatically lie 5.57 eV above the $S_{0\,min}$ (Table 2) and may provide an efficient mechanism for coupling population from an initially excited 'bright' $1^1\pi\pi^*$ state onto the optically 'dark' $^1\pi\sigma^*$ surface. This yields a predicted 'semiempirical' excitation threshold of 5.15 eV (∼241 nm) for accessing the $1^1\pi\pi^*/^1\pi\sigma^*$ CI, obtained by
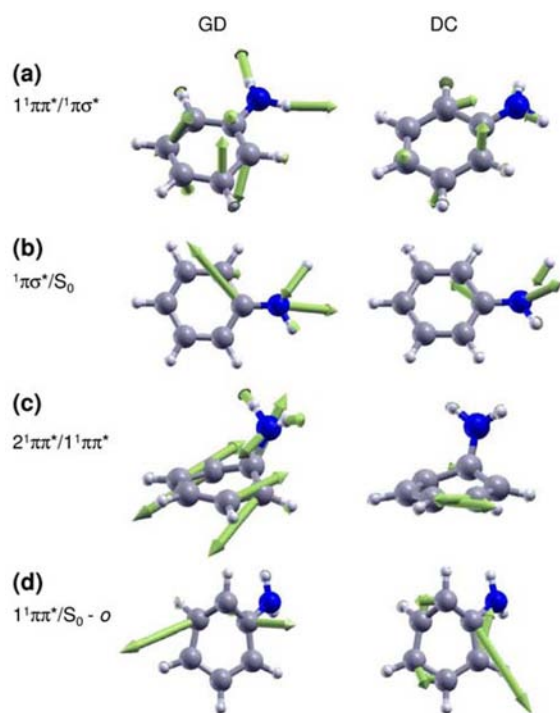
Figure 4. Calculated gradient difference (GD) and derivative coupling (DC) branching space motions associated with minimum energy crossing points of CIs in aniline.

Table 2. Calculated CASSCF Adiabatic Excitation Energies (ΔE_{ad}) for CIs in Aniline, Relative to the Calculated $S_{0\ min}$ Structure

CI	active space	ΔE_{ad}/eV
$1^1\pi\pi^*/^1\pi\sigma^*$	CAS2 (10,9)	5.57
$^1\pi\sigma^*/S_0$	CAS2 (10,9)	4.28
$2^1\pi\pi^*/1^1\pi\pi^*$	CAS1 (8,7)	5.87
$1^1\pi\pi^*/S_0\text{-}o$	CAS1 (8,7)	5.53
$1^1\pi\pi^*/S_0\text{-}m$	CAS1 (8,7)	5.50
$1^1\pi\pi^*/S_0\text{-}p$	CAS1 (8,7)	5.61

adding the adiabatic energy difference between the $1^1\pi\pi^*_{min}$ and $1^1\pi\pi^*/^1\pi\sigma^*$ CI (0.93 eV) to the experimentally determined origin of the $1^1\pi\pi^*$ state (4.22 eV). Note that due to the lack of dynamic correlation in CASSCF, this should be taken as a conservative upper-limit for the onset of $1^1\pi\pi^* \rightarrow {}^1\pi\sigma^*$ coupling. Structurally, the MECP geometry for the $1^1\pi\pi^*/^1\pi\sigma^*$ CI displays some minor out-of-plane distortion on the phenyl ring and N−H bond lengths of $R_{NH} \approx 0.98$ Å, while the near-collinear branching space vectors (156°) contain both out-of-plane motions on the aromatic ring (as previously speculated by Ashfold and co-workers)[21] and pronounced N−H stretching character.

It is useful at this stage to make a comparison with the $1^1\pi\pi^*/^1\pi\sigma^*$ CI in the isoelectronic species phenol (hydroxybenzene), which has undergone intense study in recent years.[66−68] The MECP for the $1^1\pi\pi^*/^1\pi\sigma^*$ CI in phenol occurs at a slightly elongated O−H distance ($R_{OH} = 1.2$ Å),[66,67] while in aniline it appears that the MECP between the $1^1\pi\pi^*$ and $^1\pi\sigma^*$ states is close to the equilibrium N−H bond length near the vFC region ($R_{NH} = 0.99$ Å at the $S_{0\ min}$). The variation in character between the $1^1\pi\pi^*/^1\pi\sigma^*$ CIs of the two species is likely a direct result of the different topographies of their $^1\pi\sigma^*$

surfaces: In phenol the $^1\pi\sigma^*$ surface is plateau-like around the vFC region, while in aniline it displays a strong quasi-bound profile as a result of a stronger Rydberg character through mixing with the $^1\pi$3s manifold. Ultimately, this implies that radiationless $1^1\pi\pi^* \rightarrow {}^1\pi\sigma^*$ coupling through the $1^1\pi\pi^*/^1\pi\sigma^*$ CI in aniline will drive population into the quasi-bound (3s Rydberg) well of the $^1\pi\sigma^*$ state, rather than the purely dissociative (σ^* valence) region at elongated N−H bond lengths. Such an interpretation is further supported by inspecting the optimized (state-averaged) active space orbitals at the calculated $1^1\pi\pi^*/^1\pi\sigma^*$ CI, which reveal that the N−H σ^* orbital has accumulated notable 3s Rydberg character from the N-atom. From an experimental perspective, time may therefore be required for nascent population to couple out of the quasi-bound Rydberg well and onto the dissociative region of the surface which facilitates N−H fission, culminating in an increased time scale for $^1\pi\sigma^*$ mediated H-atom elimination dynamics relative to other related heteroaromatics.[46,69,70]

For completeness, we have performed restricted CI searches between the $1^1\pi\pi^*$ and $^1\pi\sigma^*$ states away from the MECP of the $1^1\pi\pi^*/^1\pi\sigma^*$ CI, at fixed R_{NH} values of 1.1 and 1.2 Å (for one of the N−H bonds). These computations were not able to locate any degeneracies between these two states at these elongated N−H distances, indicating that the $1^1\pi\pi^*/^1\pi\sigma^*$ CI does not exist as a 'seam' along the N−H dissociation coordinate. This further suggests that direct population transfer between $1^1\pi\pi^* \rightarrow {}^1\pi\sigma^*$ does not occur at elongated N−H distances, but rather, only takes place around the MECP geometry presented in Figure 3b with respect to R_{NH}. This conclusion is also commensurate with the calculated branching space in Figure 4a, which contains N−H stretching motion, implying that movement along R_{NH} will cause the $1^1\pi\pi^*/^1\pi\sigma^*$ degeneracy to be lifted away from the MECP. The generic potential energy profiles in Figure 3a therefore show the $1^1\pi\pi^*/^1\pi\sigma^*$ CI close to the vFC region of the reaction coordinate and pictorially emphasize that there is no degeneracy between $1^1\pi\pi^*/^1\pi\sigma^*$ at elongated N−H bond lengths, indicated by the break in the $1^1\pi\pi^*$ state (solid blue lines). What is exceptionally noteworthy of this slightly unusual $1^1\pi\pi^*/^1\pi\sigma^*$ MECP is that it bears a remarkable similarity to the predicted $1^1\pi\pi^*/^1\pi\sigma^*$ electronic state degeneracy in the biologically relevant tautomer of the DNA base guanine,[71,72] strongly suggesting that aniline may indeed be an entirely adequate model for understanding $^1\pi\sigma^*$ dynamics in this ubiquitous biomolecule.

Once population has accessed the dissociative region of the $^1\pi\sigma^*$ state, our calculations reveal that population evolving along this coordinate can encounter a $^1\pi\sigma^*/S_0$ CI. We find that this $^1\pi\sigma^*/S_0$ CI (see Figures 3c and 4b for MECP geometry and branching space modes, respectively) lies at an energy of 4.28 eV above the $S_{0\ min}$ structure (Table 2). Nonadiabatic passage through this CI can, in principle, lead to either rapid N−H bond fission or repopulation of a thermally excited S_0 state, the former of which is corroborated through our TR-VMI measurements presented in Section 3.2. Structurally, this $^1\pi\sigma^*/S_0$ CI in aniline shares many similar characteristics with those of the related $^1n\sigma^*/S_0$ CI in ammonia;[2,58] in both species the CI exhibits a planar geometry ($\phi = 0°$) and occurs at significantly elongated N−H bond lengths ($R_{NH} = 1.84$ Å in aniline). The latter is an inherent characteristic of $^1\pi\sigma^*/S_0$ type CIs in aromatic heterocycles.[2,19] The branching space motions shown in Figure 4b are therefore defined by the notable rearrangement, in both the NH_2 inversion (umbrella) and N−H stretching coordinates, required to access the MECP geometry

of the $^1\pi\sigma^*/S_0$ CI from the vFC region. Both the GD and DC modes appear to be: (i) localized around the amino group; and (ii) comprised of a 'linear-combination' of the umbrella and N−H stretch motions. It is noteworthy that both of these vibrational motions have previously been shown as key mediators of ultrafast N−H fission dynamics in ammonia.[58,73]

3.1.5. CI between the $2^1\pi\pi^*/1^1\pi\pi^*$ States. At excitation energies ≥5.1 eV (∼243 nm − see experimental data in Table 1) the higher $2^1\pi\pi^*$ state may be accessed, and we investigate coupling from this state to both the lower $1^1\pi\pi^*$ and $^1\pi\sigma^*$ states. We immediately state that calculations performed using the larger CAS2 space were not able to identify any direct coupling pathways to the $^1\pi\sigma^*$ state from the $2^1\pi\pi^*$ state via a $2^1\pi\pi^*/^1\pi\sigma^*$ CI. However, using the smaller CAS1 space, we were able to determine what appears to be a near barrierless mechanism for population transfer from $2^1\pi\pi^*$ back to $1^1\pi\pi^*$. With respect to the schematic potentials in Figure 3a, following excitation to $2^1\pi\pi^*$ in the vFC region, nascent population may relax toward the $2^1\pi\pi^*_{min}$ structure, as discussed in Section 3.1.2. From this very weakly bound $2^1\pi\pi^*_{min}$, the calculations subsequently evolve toward the MECP of a $2^1\pi\pi^*/1^1\pi\pi^*$ CI, which lies at an energy of 5.87 eV relative to $S_{0\ min}$ (0.94 eV below $2^1\pi\pi^*_{min}$). The structure of this MECP geometry is provided in Figure 3d, which involves significant out-of-plane rearrangement of the NH_2 group. Associated orthogonal (96°) branching space vectors are given in Figure 4c. Interestingly, both the MECP geometry and associated branching space are very similar to those calculated for $2^1\pi\pi^*/1^1\pi\pi^*$ CIs in related 4-aminobenzonitrile systems, where the $2^1\pi\pi^*$ and $1^1\pi\pi^*$ states have VB character akin to those presented in Figure 2.[23]

The near barrierless nature of this relaxation channel from the vFC region to the $2^1\pi\pi^*/1^1\pi\pi^*$ CI is strengthened by searches for transition-state structures along the relaxation path, which do not locate any saddle point geometries. We therefore propose that after excitation to $2^1\pi\pi^*$, such a pathway could provide an efficient and ultrafast means for coupling back onto the lower lying $1^1\pi\pi^*$ surface. Once the population has been transferred into the $1^1\pi\pi^*$ state, further structural rearrangement away from the MECP geometry of the $2^1\pi\pi^*/1^1\pi\pi^*$ CI may ensue, potentially enabling access to the $1^1\pi\pi^*/^1\pi\sigma^*$ CI. Energetically, the combined CAS1 and CAS2 results suggest that the $1^1\pi\pi^*/^1\pi\sigma^*$ CI lies 0.3 eV below the $2^1\pi\pi^*/1^1\pi\pi^*$ CI. However, due to the tendency of CASSCF to overestimate ICT states (such as $2^1\pi\pi^*$), the relative energy difference between the two CIs will alter upon inclusion of dynamic correlation effects, making it difficult to determine the energetic feasibly of accessing the $1^1\pi\pi^*/^1\pi\sigma^*$ CI after coupling back onto $1^1\pi\pi^*$ through the $2^1\pi\pi^*/1^1\pi\pi^*$ CI. Although the CASSCF calculations cannot determine the likelihood of evolution from the $2^1\pi\pi^*/1^1\pi\pi^*$ CI toward the $1^1\pi\pi^*/^1\pi\sigma^*$ CI, added weight for this speculation comes through the TR-VMI results presented below, which show that ultrafast $^1\pi\sigma^*$ mediated N−H fission is active following initial excitation to the $2^1\pi\pi^*$ state.

3.1.6. Prefulvenic CIs. We finalize this section by reporting a number of prefulvenic type CIs between the $1^1\pi\pi^*/S_0$ states, which are structurally reminiscent of those calculated to play a role in the 'channel 3' relaxation dynamics of photoexcited benzene.[74] Three such CIs have been identified in aniline, whose MECP structures are shown in Figure 3e. These are labeled as *ortho* (-*o*), *meta* (-*m*), and *para* (-*p*), referring to the position of the characteristic C−H 'kink' in the benzene ring relative to the NH_2 group. The orthogonal (94°) branching space motions for the $1^1\pi\pi^*/S_0$-*o* CI are presented in Figure 4d

and are comparable to those determined for benzene's prefulvenic CI.[74] Similar branching spaces are also determined for the *m* and *p* tautomers of this CI (see Figure S3 in the SI). Energetically, the CAS1 space computes these three CIs to lie between 5.50−5.61 eV above $S_{0\ min}$ (Table 2), which is close in energy to the $1^1\pi\pi^*/^1\pi\sigma^*$ CI determined with CAS2 (5.57 eV). Above an excitation threshold of 5.50−5.61 eV these $1^1\pi\pi^*/S_0$ CIs may therefore offer a direct route for ultrafast excited-state deactivation back to S_0, which could be competitive with the sequential $1^1\pi\pi^* \rightarrow {}^1\pi\sigma^* \rightarrow S_0$ decay channel discussed in Section 3.1.4.

3.2. Time-Resolved Velocity Map Imaging. With the photochemical pathways from the ab initio calculations in mind, we now present results of ultrafast TR-VMI experiments to investigate the potentiality for $^1\pi\sigma^*$ mediated H-atom elimination dynamics in aniline following excitation at a number of significant $h\nu_{pu}$ wavelengths (λ) over the region 294−200 nm. Any subsequent H-atom photoproducts are then selectively ionized using (2 + 1) REMPI to generate H^+, with a temporally delayed fs probe pulse ($h\nu_{pr}$) centered at 243 nm. A series of H^+ velocity map images are recorded at different Δt, deconvoluted using an image reconstruction algorithm, and finally converted into the desired one-dimensional TKER spectra using an appropriate Jacobian ($R^2 \propto KE$, where R is the radius of the captured H^+ Newton spheres in the velocity map image)[75] and a TKER calibration factor.

3.2.1. Excitation around the $1^1\pi\pi^*$ Origin: $\lambda = 294$ nm. We begin by briefly discussing $^1\pi\sigma^*$ mediated dynamics following excitation around the origin of the $1^1\pi\pi^*$ state at 294 nm (4.22 eV). Consistent with earlier frequency domain studies by Ashfold and co-workers,[21] we observe no signature for N−H bond fission along the $^1\pi\sigma^*$ state at 294 nm (see the SI). Such a signature should manifest as a well-defined Gaussian signal profile in the measured time-resolved TKER spectra,[2,69] which is clearly absent in Figure S4 in the SI. This behavior is in-line with our ab initio calculations discussed above, which determine that the $1^1\pi\pi^*/^1\pi\sigma^*$ CI lies notably higher in energy than the origin of the $1^1\pi\pi^*$ state. It also implies that, unlike the isoelectronic species phenol,[67,68] no population tunnels from the origin of $1^1\pi\pi^*$ along the N−H fission coordinate and onto the $^1\pi\sigma^*$ surface near to the $^1\pi\sigma^*/S_0$ CI. We speculate that this absence of H tunneling dynamics in aniline could be due to the energy barrier being too large for tunneling. For completeness, we state that TKER spectra recorded following excitation to vibrationally excited levels in the $1^1\pi\pi^*$ state (over the 294 > λ > 270 nm range) are similar to those reported in Figure S4 in the SI.

3.2.2. Excitation around the $^1\pi\sigma^*$ Origin: $\lambda = 269.5$ nm. Both Ebata et al.[31] and King et al.[21] have reported that the origin band of the $^1\pi\sigma^*$ state lies at ∼269.5 nm (4.61 eV, see Table 1). In the latter high-resolution Rydberg tagging experiments, excitation at this wavelength results in a TKER spectrum displaying a sharp signal feature at ∼5550 cm^{-1}, in good agreement with the predicted maximum TKER (TKER$_{max}$) of ∼5470 cm^{-1} for N−H scission along the $^1\pi\sigma^*$ surface, according to

$$TKER_{max} = h\nu_{pu} - D_0 \qquad (1)$$

where $h\nu_{pu}$ is the pump photon energy (37105 cm^{-1}) and D_0 is the adiabatic N−H dissociation energy (31630 cm^{-1}).[21] By analogy with σ^* mediated H-atom elimination dynamics in alkyl-amines and ammonia,[21] the authors speculated that these H-atoms were born via tunneling from the quasi-bound

Rydberg region of the $^1\pi\sigma^*$ state to the repulsive region of this surface at elongated R_{NH}, followed by nonadiabatic dissociation through the $^1\pi\sigma^*/S_0$ CI into the C_6H_5NH ($\tilde{X}$) + H product channel, shown in Figure 3.

Figure 5 presents TKER spectra obtained from our ultrafast TR-VMI measurements at pump−probe delays of $\Delta t = -1$ ps
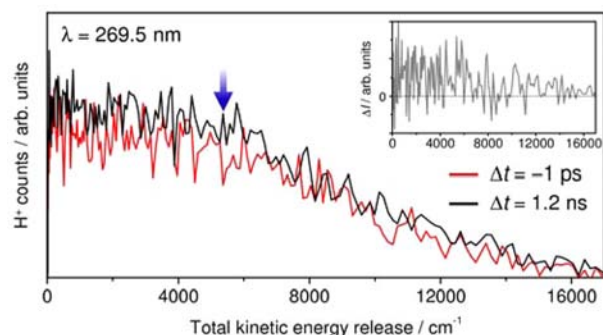

Figure 5. TKER spectra recorded at pump−probe delays (Δt) of −1 ps (red) and 1.2 ns (black) following excitation centered at 269.5 nm. Inset: Difference signal (d-TKER) spectrum obtained by subtracting the −1 ps spectrum from the 1.2 ns spectrum. The vertical blue arrow indicates the predicted maximum TKER (TKER$_{max}$, see eq 1) for signal arising from $^1\pi\sigma^*$ mediated H-atom elimination.

and 1.2 ns (red and black traces, respectively), with pump pulses centered at 269.5 nm. The H$^+$ signal at $\Delta t = -1$ ps arises exclusively from multiphoton processes following absorption of 243 nm probe photons (the origins of which are discussed in detail in the SI). The difference signal (d-TKER) spectrum inset in Figure 5 (obtained by subtracting the spectrum recorded at −1 ps from the 1.2 ns spectrum) clearly shows that, within the signal-to-noise, no Gaussian-like signature of $^1\pi\sigma^*$ induced N−H fission is observed around ~5500 cm^{-1} (vertical blue arrow). This result is contrary to the prior frequency domain measurements, and as such, we endeavor to shed some light on this discrepancy. In previous high-resolution measurements,[21] the narrow bandwidth of the ns pulses (~0.4 cm^{-1}) allows reactive flux to be purely imparted to the $v = 0$ level of the $^1\pi\sigma^*$ manifold, despite the weak one-photon oscillator strength for this transition (see Table 1). Conversely, the broadband fs pulses (~500 cm^{-1} fwhm) implemented here will distribute population across vibrational levels of the $1^1\pi\pi^*$ state, which has an oscillator strength an order of magnitude greater than the $^1\pi\sigma^*$ state (Table 1), resulting in a negligible population in the $^1\pi\sigma^*$ ($v = 0$) level and a reduced probability for H-atom elimination. This interpretation is further supported by the fact that no 'high' TKER H-atoms were observed when King et al.[21] performed excitation away from vibrational resonances in the bound region of the $^1\pi\sigma^*$ state. We do acknowledge, however, that TR-IY studies on the aniline cation signal suggest that some population can be imparted to the $^1\pi\sigma^*$ state with fs pulses.[39] Unlike our experiments though, TR-IY provides a measure of the overall population decay dynamics from the $^1\pi\sigma^*$ surface through all available relaxation mechanisms (e.g. internal conversion, fluorescence, dissociation etc.), of which H-atom elimination may not be a major decay channel. Furthermore, the kinetic analysis of these TR-IY signal transients revealed that the fraction of initial population in the $^1\pi\sigma^*$ state, relative to the $1^1\pi\pi^*$ state, is indeed minor.[39]

3.2.3. Excitation to $1^1\pi\pi^*$ above the $1^1\pi\pi^*/^1\pi\sigma^*$ CI: $\lambda =$ 250 nm. We now turn our attention to excitation at 250 nm

(4.97 eV). Inspection of the UV absorption spectrum in Figure 1 shows that there is a significantly reduced absorbance at 250 nm. In principle, either the $1^1\pi\pi^*$ or $^1\pi\sigma^*$ state may be populated in this energy region, but the larger oscillator strength of the former (see Table 1) suggests that population of the $1^1\pi\pi^*$ state is more likely.

In Figure 6a the thin red and black traces correspond to TKER spectra measured at $\Delta t = -1$ ps and 1.2 ns, respectively,
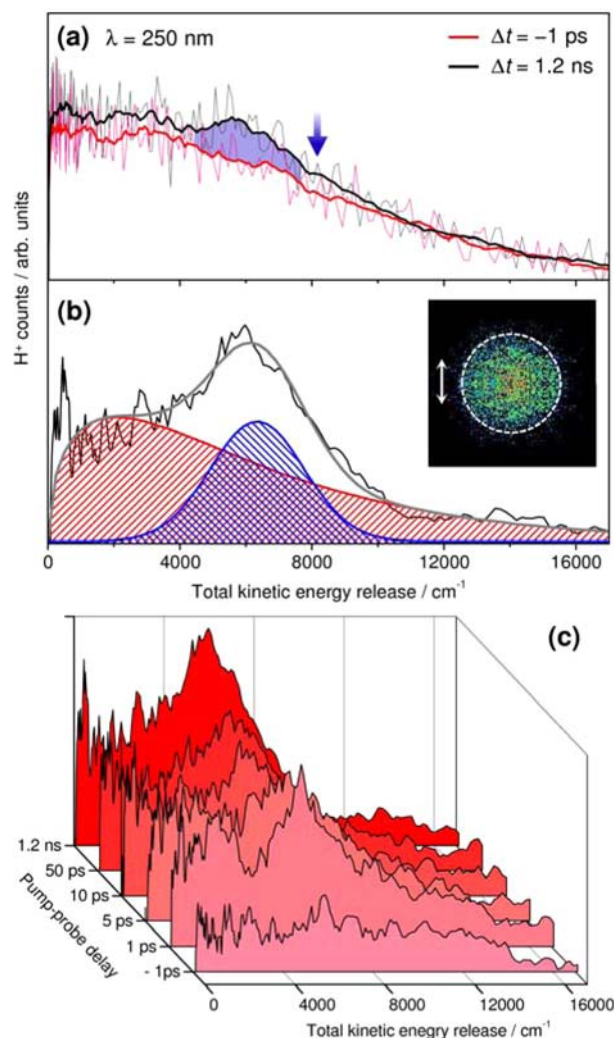

Figure 6. (a) TKER spectra recorded for excitation centered around 250 nm at $\Delta t = -1$ ps (thin red line) and 1.2 ns (thin black line). Bold lines represent a five-point average through the raw TKER spectra. (b) Five-point averaged d-TKER spectrum at 250 nm, fitted (gray line) to the sum a 'statistical' function (red shading) and a Gaussian (blue shading). Inset: pump−probe H$^+$ velocity map image from which the d-TKER spectrum is derived (white arrow indicates the pump laser polarization). (c) Time-resolved d-TKER spectra at a series of Δt following 250 nm excitation.

with a 250 nm pump, where the former results from one-color probe alone signal (see the SI). The TKER spectrum at $\Delta t = 1.2$ ns displays a notable increase in H$^+$ signal, relative to that recorded at negative Δt, particularly in the region of 5000−7000 cm^{-1} (blue shading), which is close to the predicted TKER$_{max}$ for $^1\pi\sigma^*$ mediated N−H scission (vertical blue arrow) at 250 nm. This is more clearly seen by the bold lines in Figure
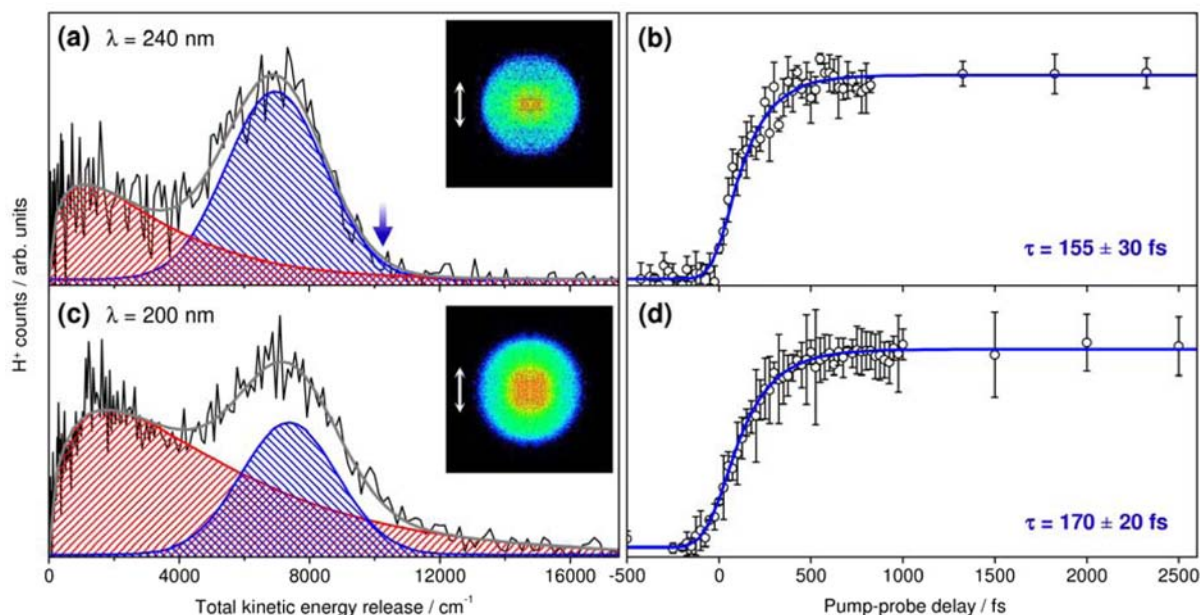
Figure 7. (a) d-TKER spectrum at $\Delta t = 1.2$ ns for 240 nm, fitted (gray line) to the sum of a 'statistical' function (red) and Gaussian (blue). Inset: pump−probe H$^+$ velocity map image from which the d-TKER spectrum is derived (white arrow = pump laser polarization). (b) H$^+$ signal transient (open circles), obtained by integrating the Gaussian fit components of the d-TKER spectrum at a series of Δt, together with an associated kinetic fit (blue line). Error bars correspond to 2 standard deviations (SD) of the mean signal values (2σ). (c) and (d) show the respective data sets following 200 nm excitation.

6a, which are obtained by performing a five-point average of the two 'raw' TKER spectra.

The d-TKER spectrum shown in Figure 6b consists purely of pump−probe H$^+$ signal. For clarity, this d-TKER spectrum represents a five-point average through the 'raw' d-TKER spectrum (not shown) obtained from the measured pump−probe H$^+$ velocity map image shown inset, which highlights the low pump−probe H$^+$ signal levels at 250 nm; counts at the center of the image correlate to low KE H$^+$, while signal at larger radii correspond to H$^+$ with higher KEs. The d-TKER spectrum contains two signal components which are heavily convoluted: an underlying 'Boltzmann-like' distribution and a Gaussian signal profile centered at ~6300 cm^{-1}. Also shown in Figure 6b is a fit to the d-TKER spectrum (gray line) using the sum of a 'statistical' function (red) and a Gaussian (blue), see the SI for fitting details. We discuss the origins of both of these components in more detail in the ensuing paragraphs.

The Gaussian feature centered at ~6300 cm^{-1} is assigned to REMPI probed H-atoms formed through $^1\pi\sigma^*$ driven N−H bond fission, on the basis that the predicted TKER$_{max}$ for this process correlates reasonably well with the high TKER tail of the Gaussian fit to this component of the d-TKER spectrum. However, what is initially less clear is the exact photophysical mechanism via which these H-atoms are formed. As noted above, absorption at 250 nm can, in principle, excite either the $1^1\pi\pi^*$ or $^1\pi\sigma^*$ states. This therefore gives rise to two possible mechanisms for N−H bond fission: (i) initial population of $1^1\pi\pi^*$ followed by rapid coupling onto $^1\pi\sigma^*$ through the calculated $1^1\pi\pi^*/^1\pi\sigma^*$ CI (Figure 3b), enabling population to evolve toward N−H fission by nonadiabatic passage through the $^1\pi\sigma^*/S_0$ CI (Figure 3c); and (ii) direct excitation to $^1\pi\sigma^*$ and passage toward the $^1\pi\sigma^*/S_0$ CI. Provided that H-atom elimination occurs on a time scale faster than rotational dephasing of the parent molecule,[75] a rigorous analysis of the angular distributions for the H$^+$ signal in the velocity map

image (associated with the high TKER Gaussian feature) has in the past enabled us to elucidate which electronic state is initially excited and isolate the correct mechanism.[46] Unfortunately here, the minimal pump−probe H$^+$ signal (see velocity map image in Figure 6b) prohibits such an analysis, as sufficient signal levels are required in the velocity map image to extract a quantitative measure of the angular distributions. In light of the larger calculated oscillator strength for the $1^1\pi\pi^* \leftarrow S_0$ transition however, we tentatively propose that the $1^1\pi\pi^* \rightarrow {}^1\pi\sigma^* \rightarrow C_6H_5NH$ ($\tilde{X}$) + H dissociation mechanism is the most feasible origin for the high TKER Gaussian feature in Figure 6b (this is also supported by the observations at 269.5 nm, where we do not observe any evidence for excitation to $^1\pi\sigma^*$). Adopting this viewpoint suggests that by 250 nm the $1^1\pi\pi^*/^1\pi\sigma^*$ CI is now accessible, which is slightly lower in energy than the ('semiempirical') predicted onset of ~240 nm for this CI in Section 3.1.4 but can be understood due to the absence of dynamic correlation in the CASSCF computations. Furthermore, this interpretation is in accord with previous analyses.[21,39]

At this stage, we concede that it has not been possible to obtain a quantitative value for the time scale of $^1\pi\sigma^*$ mediated H-atom elimination at 250 nm with TR-VMI. This is due to the small fraction of pump−probe H$^+$ signal observed from $^1\pi\sigma^*$ dynamics and the long timeframes (~2 h per image) required to record pump−probe H$^+$ images with acceptable (but small) signals. Despite these hindrances, in Figure 6c we present five-point averaged d-TKER spectra at a number of different pump−probe delays. At $\Delta t = -1$ ps there is little H$^+$ signal and no sign of a high TKER Gaussian feature around ~6300 cm^{-1}.[76] Yet, by $\Delta t = 1$ ps there is a noticeable signal increase, and in particular, the appearance of the high TKER Gaussian feature corresponding to $^1\pi\sigma^*$ driven N−H bond fission. This spectral profile remains (approximately) unaltered, as Δt is extended out to the temporal limit of our experimental setup

(Δt = 1.2 ns). From this, we are at least able to conclude that at 250 nm, the $1^1\pi\pi^* \to {}^1\pi\sigma^* \to C_6H_5NH\ (\tilde{X})$ + H dissociation mechanism in aniline is indeed ultrafast and proceeds on a time scale <1 ps.

Briefly, we consider the nature of the underlying Boltzmann-like signal in Figure 6b. We have previously ascribed such signals in other heteroaromatic systems to a combination of multiphoton processes at $\Delta t < 1$ ps.[46,70] At longer time delays, we have also observed increases in these Boltzmann-like signals, occurring over a time scale of hundreds of ps, which we attributed to the onset of 'statistical' unimolecular H-atom elimination from a vibrationally hot S_0 state[7] (after excitation, hot S_0 species can be formed by coupling back onto S_0 through appropriate CIs). In aniline we similarly observe this feature to appear within a time frame of <1 ps (see Figure 6c) and therefore assign this 'ultrafast' Boltzmann-like signal to multiphoton effects (e.g., dissociative ionization). Our CASSCF calculations also suggest that it may be feasible to form hot S_0 species, through either one of the three available $1^1\pi\pi^*/S_0$ prefulvenic CIs (Figure 3e) or via a cascade process through $1^1\pi\pi^*/{}^1\pi\sigma^* \to {}^1\pi\sigma^*/S_0$ CIs, noting that the energetic onsets for these channels are calculated to be similar (see Table 2). However, within the limited signal-to-noise of the measured d-TKER spectra in Figure 6c, no increase in the amplitude of the Boltzmann-like signal is observed (out to Δt = 1.2 ns), leading us to speculate that maybe: (i) only a minimal fraction of excited-state population couples back into a hot S_0 species; (ii) upon accessing the ${}^1\pi\sigma^*/S_0$ CI, the majority of population couples into the N−H dissociation channel; and (iii) coupling back to S_0 through the $1^1\pi\pi^*/S_0$ prefulvenic CIs is only a minor channel in aniline. Alternatively, we acknowledge that statistical unimolecular H-atom elimination from hot S_0 may be slower in aniline than the hundreds of ps time frame we have previously reported.[7] Similar temporal behavior is also observed for the Boltzmann-like signal at all subsequent excitation wavelengths, and we therefore do not discuss these features any further.

3.2.4. Dynamics Following Short Wavelength Excitation: $\lambda \leq 240$ nm. Upon exciting with the shorter wavelength of 240 nm (5.17 eV) population will primarily be imparted to the higher lying $2^1\pi\pi^*$ surface, which possesses an oscillator strength 1−2 orders of magnitude greater than the $1^1\pi\pi^*$ and ${}^1\pi\sigma^*$ states, respectively (see Table 1). This is confirmed by the onset of an absorption increase at ∼240 nm in the UV absorption spectrum (Figure 1). Analogous to previous excitation wavelengths, a d-TKER spectrum is generated following excitation at 240 nm, presented in Figure 7a (associated pump−probe H$^+$ velocity map image inset), which continues to exhibit convoluted Boltzmann-like and Gaussian signal profiles. A fit to this d-TKER spectrum (gray line) highlights that the extremely high TKER tail for this Gaussian feature (blue shading) coincides reasonably well with the predicted TKER$_{max}$ for REMPI probed H-atoms generated via N−H dissociation along the ${}^1\pi\sigma^*$ state at 240 nm (vertical blue arrow). The mean TKER of this Gaussian signal profile, however, occurs at lower TKER (∼7200 cm^{-1}). This arises because the ${}^1\pi\sigma^*$ surface is not purely repulsive but has a strong quasi-bound character around the vFC region. With this in mind, the mean TKER correlates to the energy difference between the barrier formed through the interaction of the 3s Rydberg and the σ^* characters of this state and the diabatic dissociation asymptote of the ${}^1\pi\sigma^*$ state, labeled δE on the schematic potentials in Figure 3a.[77,78]

Unlike the experiments performed at 250 nm, the pump−probe H$^+$ signal levels following excitation at 240 nm are sufficient to extract a more definitive time scale for ${}^1\pi\sigma^*$ driven H-atom elimination. Specifically, this is achieved by generating a series of d-TKER spectra at different Δt and then fitting each individual spectrum to the sum of a 'statistical' distribution and a Gaussian function (as exemplified in Figure 7a). At each Δt, the Gaussian fit component is integrated to generate the H$^+$ signal transient shown in Figure 7b (open circles), which correlates to the appearance of REMPI probed H-atoms generated via the ${}^1\pi\sigma^*$ surface. A kinetic fit to this experimental transient (blue line), using a single exponential rise function convoluted with our Gaussian instrument response (∼120 fs fwhm, see Section 2.1), provides an appearance time constant, τ, for H-atoms generated along the ${}^1\pi\sigma^*$ surface of 155 ± 30 fs (see the SI for kinetic fit details).

The H-atom elimination lifetime extracted from the transient in Figure 7b is comparable, within measured error bars, to the previously obtained ${}^1\pi\sigma^*$ state lifetime at 240 nm using TR-IY ($\tau = 165 \pm 30$ fs).[39] Within the context of our CASSCF calculations (Section 3.1.5) and remembering that they do not identify a direct CI between the $2^1\pi\pi^*$ and ${}^1\pi\sigma^*$ surfaces, the ultrafast appearance of the high TKER H-atoms measured through Figure 7b strongly supports a near barrierless (and extremely rapid) pathway to coupling at the $2^1\pi\pi^*/1^1\pi\pi^*$ CI from the vFC region of the $2^1\pi\pi^*$ state. A further ultrafast process then ensues to enable coupling through the $1^1\pi\pi^*/{}^1\pi\sigma^*$ CI, causing population to evolve along the ${}^1\pi\sigma^*$ state toward the ${}^1\pi\sigma^*/S_0$ CI and result in N−H bond fission. The comparability between our measured H-atom elimination time constant and the previously determined ${}^1\pi\sigma^*$ lifetime at 240 nm[39] strongly implies that coupling onto the ${}^1\pi\sigma^*$ surface from the initially excited $2^1\pi\pi^*$ state is extremely rapid (on the order of tens of fs). We therefore attribute the measured 155 ± 30 fs time constant to the time taken for the overall $2^1\pi\pi^* \to 1^1\pi\pi^* \to {}^1\pi\sigma^* \to C_6H_5NH\ (\tilde{X})$ + H mechanism to occur, as mediated via the appropriate CIs shown in Figure 3.

Finally, we present results following excitation to the high-energy $3^1\pi\pi^*$ manifold at 200 nm (6.21 eV). Although there are a number of Rydberg states calculated to lie in close proximity to $3^1\pi\pi^*$,[36] their oscillator strengths are all 1−2 orders of magnitude smaller than the $3^1\pi\pi^*$ state (see Table 1), making it highly improbable that any significant population will be initially imparted to them. In Figure 7c,d the fitted d-TKER spectrum and the H$^+$ signal transient for the fitted Gaussian signal component are presented, respectively. Using the same kinetic fitting process described above, fits to this high TKER H$^+$ signal transient yield a time constant of $\tau = 170 \pm 20$ fs for N−H bond fission along the ${}^1\pi\sigma^*$ state following initial population of $3^1\pi\pi^*$. This is comparable to the ultrafast ${}^1\pi\sigma^*$ driven N−H bond fission time scale following relaxation from the lower energy $2^1\pi\pi^*$ at 240 nm. Unfortunately, identifying the exact CIs which can facilitate coupling back to the ${}^1\pi\sigma^*$ state from $3^1\pi\pi^*$ using CASSCF is significantly complicated by the greatly increased density of electronic states in this higher excitation region. As such, it is not possible for us to make a certain assignment of the mechanism leading to ultrafast ${}^1\pi\sigma^*$ mediated N−H fission at 200 nm. We may postulate that these ultrafast N−H fission dynamics are facilitated through either: (i) a cascade of couplings at appropriate CIs, such as those discussed for excitation at 240 nm; or (ii) dynamics at 200 nm may alternatively proceed directly through a $3^1\pi\pi^*/{}^1\pi\sigma^*$ CI. Given that the measured τ following excitation to the $2^1\pi\pi^*$

and $3^1\pi\pi^*$ states is similar, this may garner more support for the former of these mechanisms, where the initial step proceeds via a $3^1\pi\pi^*/2^1\pi\pi^*$ CI.

4. CONCLUSIONS

In this investigation we have presented a thorough computational analysis of CIs which can play a role in the excited-state photochemistry of the model heteroaromatic system, aniline, alongside detailed ultrafast time-resolved velocity map imaging measurements which focus on the role of $^1\pi\sigma^*$ mediated dynamics along the NH_2 moiety, by monitoring time scales for H-atom elimination. Unlike previous works, this synergy between experiment and theory has enabled a much more rigorous picture of the photochemical pathways leading to ultrafast $^1\pi\sigma^*$ driven dynamics to be constructed. Specifically, following excitation with broadband fs pulses to the $1^1\pi\pi^*$ excited electronic state at >250 nm, we do not find any evidence of $^1\pi\sigma^*$ promoted N−H bond fission. However, we note that under appropriate experimental conditions (direct excitation to $^1\pi\sigma^*$ with narrow band laser pulses), it has previously been shown that $^1\pi\sigma^*$ promoted N−H bond fission can be observed at wavelengths as long as 269.5 nm,[21] in accord with our present theory. At 250 nm, coupling onto the $1^1\pi\pi^*/^1\pi\sigma^*$ CI is an open pathway, enabling $^1\pi\sigma^*$ driven N−H scission to take place through the $^1\pi\sigma^*/S_0$ CI in <1 ps. Following shorter wavelength excitation (240 nm) to the $2^1\pi\pi^*$ state, ultrafast N−H bond fission persists, taking place on a time scale of 155 ± 30 fs. Here, near barrierless access to a $2^1\pi\pi^*/1^1\pi\pi^*$ CI allows ultrafast population transfer back to $1^1\pi\pi^*$ followed by sequential coupling at the $1^1\pi\pi^*/^1\pi\sigma^*$ and $^1\pi\sigma^*/S_0$ CIs. Analogous H-atom elimination dynamics is finally observed at 200 nm through population of the higher lying $3^1\pi\pi^*$ state, which we envisage evolves through a similar photochemical pathway to that described at 240 nm in 170 ± 30 fs.

Aniline and its chemical derivatives have previously been seen as simple models for understanding $^1\pi\sigma^*$ dynamics along the NH_2 group of the purine derived DNA bases. Our calculations particularly allude to the fact that the relative electronic state orderings, and the characteristics of the $1^1\pi\pi^*/^1\pi\sigma^*$ CI bear some heavy resemblances with the calculated excited-state potential energy landscape around the amino moiety in the biologically relevant tautomer of guanine.[71,72] This suggests that the novel studies presented here could possibly provide grounds for building toward a greater understanding of $^1\pi\sigma^*$ dynamics in this isolated DNA base, which, relative to adenine, has been comparatively understudied. We envisage that these experimental studies on aniline can promote a move toward understanding $^1\pi\sigma^*$ photochemistry in guanine, proceeding in a logical stepwise fashion via investigations into any evolution of the $^1\pi\sigma^*$ behavior in amino substituted pyrimidines and eventually guanine with more appropriate gas-phase laser desorption techniques.[79]

ASSOCIATED CONTENT

Ⓢ Supporting Information

Further experimental details, fitting procedure for H^+ signal transients, CASSCF active space orbitals, spin-exchange density and localized one-electron density matrix elements, prefulvenic branching space vectors, calculated CASSCF Cartesian geometries and absolute energies, time-resolved TKER spectra at 294 nm and multiphoton background, and complete refs 47 and 48. This material is available free of charge via the Internet at http://pubs.acs.org.

AUTHOR INFORMATION

Corresponding Author

v.stavros@warwick.ac.uk; m.j.paterson@hw.ac.uk

Notes

The authors declare no competing financial interest.

REFERENCES

(1) Ashfold, M. N. R.; Cronin, B.; Devine, A. L.; Dixon, R. N.; Nix, M. G. D. *Science* **2006**, *312*, 1637−1640.
(2) Ashfold, M. N. R.; King, G. A.; Murdock, D.; Nix, M. G. D.; Oliver, T. A. A.; Sage, A. G. *Phys. Chem. Chem. Phys.* **2010**, *12*, 1218−1238.
(3) Crespo-Hernandez, C. E.; Cohen, B.; Hare, P. M.; Kohler, B. *Chem. Rev.* **2004**, *104*, 1977−2019.
(4) Middleton, C. T.; de La Harpe, K.; Su, C.; Law, Y. K.; Crespo-Hernandez, C. E.; Kohler, B. *Annu. Rev. Phys. Chem.* **2009**, *60*, 217−239.
(5) Schreier, W. J.; Schrader, T. E.; Koller, F. O.; Gilch, P.; Crespo-Hernandez, C. E.; Swaminathan, V. N.; Carell, T.; Zinth, W.; Kohler, B. *Science* **2007**, *315*, 625−629.
(6) Balucani, N. *Int. J. Mol. Sci.* **2009**, *10*, 2304−2335.
(7) Roberts, G. M.; Williams, C. A.; Paterson, M. J.; Ullrich, S.; Stavros, V. G. *Chem. Sci.* **2012**, *3*, 1192−1199.
(8) Ullrich, S.; Schultz, T.; Zgierski, M. Z.; Stolow, A. *J. Am. Chem. Soc.* **2004**, *126*, 2262−2263.
(9) Ullrich, S.; Schultz, T.; Zgierski, M. Z.; Stolow, A. *Phys. Chem. Chem. Phys.* **2004**, *6*, 2796−2801.
(10) Satzger, H.; Townsend, D.; Zgierski, M. Z.; Patchkovskii, S.; Ullrich, S.; Stolow, A. *Proc. Natl. Acad. Sci. U.S.A.* **2006**, *103*, 10196−10201.
(11) Nix, M. G. D.; Devine, A. L.; Cronin, B.; Ashfold, M. N. R. *J. Chem. Phys.* **2007**, *126*, 124312.
(12) Evans, N. L.; Ullrich, S. *J. Phys. Chem. A* **2010**, *114*, 11225−11230.
(13) Iqbal, A.; Stavros, V. G. *J. Phys. Chem. Lett.* **2010**, *1*, 2274−2278.
(14) Crespo-Hernandez, C. E.; Cohen, B.; Kohler, B. *Nature* **2005**, *436*, 1141−1144.
(15) Schwalb, N. K.; Temps, F. *J. Am. Chem. Soc.* **2007**, *129*, 9272−9273.
(16) Kohler, B. *J. Phys. Chem. Lett.* **2010**, *1*, 2047−2053.
(17) Wells, K. L.; Hadden, D. J.; Nix, M. G. D.; Stavros, V. G. *J. Phys. Chem. Lett.* **2010**, *1*, 993−996.
(18) *Conical Intersections: Theory, Computation and Experiment*; Domcke, W., Yarkony, D. R., Koppel, H., Eds.; World Scientific: New Jersey, 2011; Vol. 17.
(19) Sobolewski, A. L.; Domcke, W.; Dedonder-Lardeux, C.; Jouvet, C. *Phys. Chem. Chem. Phys.* **2002**, *4*, 1093−1100.

12588

dx.doi.org/10.1021/ja3029729 | *J. Am. Chem. Soc.* 2012, 134, 12578−12589

(20) Barbatti, M.; Aquino, A. J. A.; Szymczak, J. J.; Nachtigallova, D.; Hobza, P.; Lischka, H. *Proc. Natl. Acad. Sci. U.S.A.* **2010**, *107*, 21453−21458.

(21) King, G. A.; Oliver, T. A. A.; Ashfold, M. N. R. *J. Chem. Phys.* **2010**, *132*, 214307.

(22) Schultz, T.; Samoylova, E.; Radloff, W.; Hertel, I. V.; Sobolewski, A. L.; Domcke, W. *Science* **2004**, *306*, 1765−1768.

(23) Gomez, I.; Reguero, M.; Boggio-Pasqua, M.; Robb, M. A. *J. Am. Chem. Soc.* **2005**, *127*, 7119−7129.

(24) Sudholt, W.; Sobolewski, A. L.; Domcke, W. *Chem. Phys.* **1999**, *240*, 9−18.

(25) Grabowski, Z. R.; Rotkiewicz, K.; Rettig, W. *Chem. Rev.* **2003**, *103*, 3899−4031.

(26) Lister, D. G.; Tyler, J. K.; Hog, J. H.; Larsen, N. W. *J. Mol. Struct.* **1974**, *23*, 253−264.

(27) Bacon, A. R.; Hollas, J. M. *Faraday Discuss.* **1988**, *86*, 129−141.

(28) Sinclair, W. E.; Pratt, D. W. *J. Chem. Phys.* **1996**, *105*, 7942−7956.

(29) Yeh, J. H.; Shen, T. L.; Nocera, D. G.; Leroi, G. E.; Suzuka, I.; Ozawa, H.; Namuta, Y. *J. Phys. Chem.* **1996**, *100*, 4385−4389.

(30) Spoerel, U.; Stahl, W. *J. Mol. Spectrosc.* **1998**, *190*, 278−289.

(31) Ebata, T.; Minejima, C.; Mikami, N. *J. Phys. Chem. A* **2002**, *106*, 11070−11074.

(32) Tseng, C. M.; Dyakov, Y. A.; Huang, C. L.; Mebel, A. M.; Lin, S. H.; Lee, Y. T.; Ni, C. K. *J. Am. Chem. Soc.* **2004**, *126*, 8760−8768.

(33) Bock, C. W.; George, P.; Trachtman, M. *Theor. Chim. Acta* **1986**, *69*, 235−245.

(34) Bludsky, O.; Sponer, J.; Leszczynski, J.; Spirko, V.; Hobza, P. *J. Chem. Phys.* **1996**, *105*, 11042−11050.

(35) Lopez-Tocon, I.; Della Valle, R. G.; Becucci, M.; Castellucci, E.; Otero, J. C. *Chem. Phys. Lett.* **2000**, *327*, 45−53.

(36) Honda, Y.; Hada, M.; Ehara, M.; Nakatsuji, H. *J. Chem. Phys.* **2002**, *117*, 2045−2052.

(37) Wojciechowski, P. M.; Zierkiewicz, W.; Michalska, D.; Hobza, P. *J. Chem. Phys.* **2003**, *118*, 10900−10911.

(38) Alabugin, I. V.; Manoharan, M.; Buck, M.; Clark, R. J. *J. Mol. Struct. (THEOCHEM)* **2007**, *813*, 21−27.

(39) Montero, R.; Conde, A. P.; Ovejas, V.; Martinez, R.; Castano, F.; Longarte, A. *J. Chem. Phys.* **2011**, *135*, 054308.

(40) Since the submission of this article, two ultrafast time-resolved photoelectron spectroscopy studies investigating excited-state dynamics in aniline have been published. See: Spesyvtsev, R.; Kirkby, O. M.; Vacher, M.; Fielding, H. H. *Phys. Chem. Chem. Phys.* **2012**, *14*, 9942−9947. Spesyvtsev, R.; Kirkby, O. M.; Fielding, H. H. *Faraday Discuss.* **2012**, DOI: 10.1039/C2FD20076G.

(41) Zewail, A. H. *J. Phys. Chem. A* **2000**, *104*, 5660−5694.

(42) Eppink, A. T. J. B.; Parker, D. H. *Rev. Sci. Instrum.* **1997**, *68*, 3477−3484.

(43) Wells, K. L.; Perriam, G.; Stavros, V. G. *J. Chem. Phys.* **2009**, *130*, 074304.

(44) Even, U.; Jortner, J.; Noy, D.; Lavie, N.; Cossart-Magos, C. *J. Chem. Phys.* **2000**, *112*, 8068−8071.

(45) Roberts, G. M.; Nixon, J. L.; Lecointre, J.; Wrede, E.; Verlet, J. R. R. *Rev. Sci. Instrum.* **2009**, *80*, 053104.

(46) Williams, C. A.; Roberts, G. M.; Yu, H.; Evans, N. L.; Ullrich, S.; Stavros, V. G. *J. Phys. Chem. A* **2012**, *116*, 2600−2609.

(47) Frisch, M. J.; et al. *Gaussian 03*, revision D.01; Gaussian, Inc.: Wallingford, CT, 2004.

(48) Frisch, M. J.; et al. *Gaussian 09*, revision A.02; Gaussian, Inc.: Wallingford, CT, 2009.

(49) Stanton, J. F.; Bartlett, R. J. *J. Chem. Phys.* **1993**, *98*, 7029−7039.

(50) Yanai, T.; Tew, D. P.; Handy, N. C. *Chem. Phys. Lett.* **2004**, *393*, 51−57.

(51) Tozer, D. J.; Handy, N. C. *J. Chem. Phys.* **1998**, *109*, 10180−10189.

(52) Tozer, D. J.; Amos, R. D.; Handy, N. C.; Roos, B. O.; Serrano-Andres, L. *Mol. Phys.* **1999**, *97*, 859−868.

(53) Bernardi, F.; Celani, P.; Olivucci, M.; Robb, M. A.; Suzzivalli, G. *J. Am. Chem. Soc.* **1995**, *117*, 10531−10536.

(54) Boys, S. F. *Rev. Mod. Phys.* **1960**, *32*, 296−299.

(55) Blancafort, L.; Celani, P.; Bearpark, M. J.; Robb, M. A. *Theor. Chem. Acc.* **2003**, *110*, 92−99.

(56) Paterson, M. J.; Robb, M. A.; Blancafort, L.; DeBellis, A. D. *J. Am. Chem. Soc.* **2004**, *126*, 2912−2922.

(57) Paterson, M. J.; Robb, M. A.; Blancafort, L.; DeBellis, A. D. *J. Phys. Chem. A* **2005**, *109*, 7527−7537.

(58) Hause, M. L.; Yoon, Y. H.; Crim, F. F. *J. Chem. Phys.* **2006**, *125*, 174309.

(59) Experimentally determined rotational constants for the $1^1\pi\pi*$ state in aniline are A = 5276.9 MHz, B = 2633.8 MHz, and C = 1759.4 MHz, determined in ref 28. Rotational constants for the calculated $1^1\pi\pi*_{min}$ structure in Figure 2b are A = 5322.6 MHz, B = 2562.2 MHz, and C = 1731.9 MHz, yielding differences of ΔA = +45.7 MHz, ΔB = −71.5 MHz, and ΔC = −27.5 MHz relative to the experimental values.

(60) Serrano-Andres, L.; Roos, B. O. *J. Am. Chem. Soc.* **1996**, *118*, 185−195.

(61) Klene, M.; Robb, M. A.; Blancafort, L.; Frisch, M. J. *J. Chem. Phys.* **2003**, *119*, 713−728.

(62) Paterson, M. J.; Bearpark, M. J.; Robb, M. A.; Blancafort, L. *J. Chem. Phys.* **2004**, *121*, 11562−11571.

(63) Blancafort, L.; Gonzalez, D.; Olivucci, M.; Robb, M. A. *J. Am. Chem. Soc.* **2002**, *124*, 6398−6406.

(64) Wilsey, S.; Houk, K. N. *J. Am. Chem. Soc.* **2000**, *122*, 2651−2652.

(65) Yarkony, D. R. *Rev. Mod. Phys.* **1996**, *68*, 985−1013.

(66) Vieuxmaire, O. P. J.; Lan, Z.; Sobolewski, A. L.; Domcke, W. *J. Chem. Phys.* **2008**, *129*, 224307.

(67) Dixon, R. N.; Oliver, T. A. A.; Ashfold, M. N. R. *J. Chem. Phys.* **2011**, *134*, 194303.

(68) Roberts, G. M.; Chatterley, A. S.; Young, J. D.; Stavros, V. G. *J. Phys. Chem. Lett.* **2012**, *3*, 348−352.

(69) Iqbal, A.; Cheung, M. S. Y.; Nix, M. G. D.; Stavros, V. G. *J. Phys. Chem. A* **2009**, *113*, 8157−8163.

(70) Hadden, D. J.; Wells, K. L.; Roberts, G. M.; Bergendahl, L. T.; Paterson, M. J.; Stavros, V. G. *Phys. Chem. Chem. Phys.* **2011**, *13*, 10342−10349.

(71) Yamazaki, S.; Domcke, W.; Sobolewski, A. L. *J. Phys. Chem. A* **2008**, *112*, 11965−11968.

(72) Yamazaki, S.; Domcke, W. *J. Phys. Chem. A* **2008**, *112*, 7090−7097.

(73) Evans, N. L.; Yu, H.; Roberts, G. M.; Stavros, V. G.; Ullrich, S. *Phys. Chem. Chem. Phys.* **2012**, *14*, 10401−10409.

(74) Palmer, I. J.; Ragazos, I. N.; Bernardi, F.; Olivucci, M.; Robb, M. A. *J. Am. Chem. Soc.* **1993**, *115*, 673−682.

(75) *Imaging in Molecular Dynamics: Technology and Applications.* Whitaker, B. J., Ed.; Cambridge University Press: Cambridge, UK, 2003.

(76) We highlight that the d-TKER spectra presented in Figure 6c were obtained by subtracting a spectrum recorded at Δt = −5 ps from those recorded at the presented Δt values. As a result of the poor signal-to-noise levels at 250 nm, the d-TKER spectrum presented at Δt = −1 ps displays a small amount of signal. This is due to small signal differences between the Δt = −1 and −5 ps.

(77) Devine, A. L.; Cronin, B.; Nix, M. G. D.; Ashfold, M. N. R. *J. Chem. Phys.* **2006**, *125*, 184302.

(78) Cronin, B.; Nix, M. G. D.; Qadiri, R. H.; Ashfold, M. N. R. *Phys. Chem. Chem. Phys.* **2004**, *6*, 5031−5041.

(79) Smits, M.; de Lange, C. A.; Ullrich, S.; Schultz, T.; Schmitt, M.; Underwood, J. G.; Shaffer, J. P.; Rayner, D. M.; Stolow, A. *Rev. Sci. Instrum.* **2003**, *74*, 4812−4817.